ChemComm

COMMUNICATION

View Article Online
View Journal | View Issue

Check for updates

Cite this: *Chem. Commun.*, 2024, **60**, 14276

Received 29th September 2024, Accepted 5th November 2024

DOI: 10.1039/d4cc05090h

rsc.li/chemcomm

Published on 06 November 2024. Downloaded on 3/3/2026 11:38:33 PM.

Anatase/TiO_2(B) homojunction nanosheets with a gold cocatalyst for direct photocatalytic coupling of methane to ethane†

Xuanzhao Lu,‡[b] Huanhuan Luo,‡[b] Biyang Xu,‡[b] Zhuo Liu,‡[b] Yue Cao,[a] Kai Li,[c] Xiaohan Yang,[b] Liangyiqun Xie,[b] Tao Guan,[b] Wenlei Zhu *[b] and Yang Zhou *[a]

An anatase/TiO_2(B) homojunction loaded with Au nanoparticles was synthesized, achieving a C_2H_6 yield rate of 170 μmol g^{-1} h^{-1} in a flow photoreactor. The homojunction reduces TiO_2(B)'s strong oxidative ability, offering a more moderate environment for methane dehydrogenation, while Au aids in charge mitigation and methyl radical coupling. The catalyst highlights homojunction engineering and a ternary synergistic effect in photocatalytic CH_4 coupling.

The efficient conversion of methane (CH_4) into valuable products can help mitigate the greenhouse effect while generating useful chemicals.[1–6] The non-oxidative coupling of methane (NOCM) can convert CH_4 to C2 hydrocarbons (such as ethane (C_2H_6)) directly. However, this reaction is thermodynamically unfavorable owing to the high C–H bond energy, low polarizability, and poor electron affinity of CH_4, which requires a huge energy input and harsh reaction conditions for the first C–H bond breakage.[7] Therefore, developing sustainable strategies for cleaner and more cost-effective NOCM routes is essential.

Photocatalysts can reduce the activation energy of CH_4 dehydrogenation more easily than thermal catalysts, thereby enabling CH_4 coupling under mild conditions.[8–10] Noble metals are considered as promising co-catalysts for promoting CH_4 coupling, and Au is the most effective owing to its relatively higher C_2H_6 selectivity.[11,12] However, small-sized unsupported Au nanoparticles (NPs) are thermodynamically unstable and prone to agglomeration due to their high surface energy. Hence, appropriate supports are required to achieve a balance between the dispersion and stability of the Au NPs.

Bulk TiO_2 is a well-studied photocatalyst for NOCM, but it struggles with poor photogenerated electron–hole pair separation capacity and scarce CH_4 adsorption sites, reducing its photocatalytic performance.[13–15] Two-dimensional TiO_2 provides sufficient sites for CH_4 adsorption, and its atomic-level thickness facilitates the efficient short-distance diffusion of carriers to the catalyst surface.[16,17] TiO_2(B) is a polymorph of TiO_2. Recently, TiO_2(B) nanosheets (NSs) have attracted attention in photocatalysis because of their relatively high specific surface area and inherent defect-rich surface properties. These features provide an ideal platform for the surface nucleation of noble metals, enabling dispersed cocatalyst loading or heterogeneous structure modification.[18,19]

In this work, a TiO_2(B)-anatase homojunction catalyst loaded with Au NPs was synthesized and the optimal C_2H_6 yield rate reached 170 μmol g^{-1} h^{-1} in a flow-cell photocatalytic system. We found that the photocatalyst composed of Au, TiO_2(B), and anatase exhibited a ternary synergistic effect, which enhanced the overall photocatalytic activity. The *in situ* conversion of TiO_2(B) to anatase TiO_2 allows the formation of closely contacted TiO_2 type-II homojunctions, creating a more moderate environment for CH_4 dehydrogenation and coupling compared to the initial TiO_2(B) NSs. In addition, the participation of Au not only further improves the separation of electron–hole pairs but also helps to capture some methyl intermediates, alleviating the excessive oxidation of CH_4 to CO_2, thus resulting in improved C_2H_6 production.

The synthesis processes of Au–Ti300 are illustrated in Fig. 1(a). The anatase phase was introduced into the TiO_2(B) phase by calcining the TiO_2(B) NSs at 300 °C, resulting in the sample designated as Ti300. Scanning electron microscopy (SEM) images (Fig. S1 and S2, ESI†) reveal that the nanosheet morphology of $Au_{1.0}$–Ti300 remains largely unchanged after heat treatment. UV-Vis diffuse reflectance spectroscopy (DRS; Fig. S3, ESI†) indicates enhanced visible light absorbance for Ti300 due to the TiO_2(B)–anatase junction and confirms the presence of Au NPs through an absorption peak at ∼560 nm.[20]

[a] *State Key Laboratory for Organic Electronics and Information Displays & Institute of Advanced Materials (IAM), Nanjing University of Posts & Telecommunications, Nanjing 210023, China. E-mail: iamyangzhou@njupt.edu.cn*

[b] *State Key Laboratory of Pollution Control and Resource Reuse, State Key Laboratory of Analytical Chemistry for Life Science, Frontiers Science Center for Critical Earth Material Cycling, School of Chemistry and Chemical Engineering, School of the Environment, Nanjing University, Nanjing 210023, China. E-mail: wenleizhu@nju.edu.cn*

[c] *School of Science, Wuhan University of Science and Technology, Wuhan 430065, China*

† Electronic supplementary information (ESI) available. See DOI: https://doi.org/10.1039/d4cc05090h

‡ These authors contributed equally to this work.

This journal is © The Royal Society of Chemistry 2024

Published on 06 November 2024. Downloaded on 3/3/2026 11:38:33 PM.

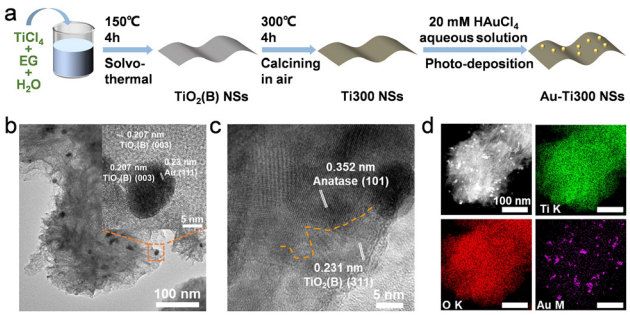

Fig. 1 (a) Schematic illustration of the preparation of Au–Ti300. (b) TEM image of $Au_{1.0}$–Ti300. The enlarged image of the selected area (inset). (c) HRTEM image of $Au_{1.0}$–Ti300. (d) STEM image of $Au_{1.0}$–Ti300 and corresponding element mapping (Ti, O, and Au).

Transmission electron microscopy (TEM) images reveal the wrinkled ultrathin morphology of TiO_2 NSs (Fig. S4, ESI†), which remains unchanged after calcination (Fig. 1(b)). Au NPs were evenly distributed on Ti300, averaging 9.77 nm in diameter (Fig. S5, ESI†). The actual loading of Au on the TiO_2 samples was quantified using inductively coupled plasma–optical emission spectroscopy (ICP-OES; Table S1, ESI†). The high-resolution TEM (HRTEM) image (Fig. 1(c)) shows lattice spacings of 0.352 and 0.231 nm, corresponding to the anatase TiO_2 (101) and TiO_2(B) (311) planes, respectively. A close-contact interface (marked by the orange dashed line) between the two phases suggests the formation of a homojunction between the anatase and TiO_2(B) phase, potentially enhancing charge transfer over the phase interfaces. Another HRTEM image (Fig. 1(b), inset) shows lattice spacings of 0.207 and 0.230 nm, corresponding to TiO_2(B) (003) and Au (111), respectively. Scanning TEM (STEM) and the corresponding energy-dispersive X-ray spectroscopy (EDS) elemental mapping images (Fig. 1(d)) reveal that Ti, O, and Au are homogenously distributed throughout $Au_{1.0}$–Ti300.

X-ray diffraction (XRD) was employed to investigate the phase transformations of the crystals (Fig. 2(a) and Fig. S6, ESI†). The diffraction peaks of the pristine TiO_2(B) NSs match well with those of the pure TiO_2(B) phase (JCPDS no. 46-1238). Phase transformations of TiO_2 crystals occurred during calcination;[21] notably, an anatase (101) peak at 25.3° appeared in Ti400 (Fig. S6, ESI†), accompanied by the gradual disappearance of the TiO_2(B) phase and the aggregation of the NSs into larger particles. By Ti500 and Ti600, TiO_2(B) was completely converted into pure anatase. With the further increase of the calcination temperature above 700 °C, the anatase phase is further converted to the rutile phase (JCPDS no. 21-1276). For Ti300, characteristic peaks of the anatase phase (JCPDS no. 21-1272) were observed, and the red-shift of the peak from 24.9° to 25.1° indicated the existence of mixed TiO_2 crystal phases on Ti300, consistent with the HRTEM results. Because of the low crystallinity and adjacent diffraction peaks of anatase and TiO_2(B), it was difficult to obtain the exact anatase/TiO_2(B) phase ratio for Ti300. However, the TiO_2(B) phase was still the dominant component of Ti300 based on the existence of a peak assigned to TiO_2(B) (003) at 43.5° after calcination. XRD analysis also shows Au peaks but no incorporation of Au into the TiO_2 lattice.

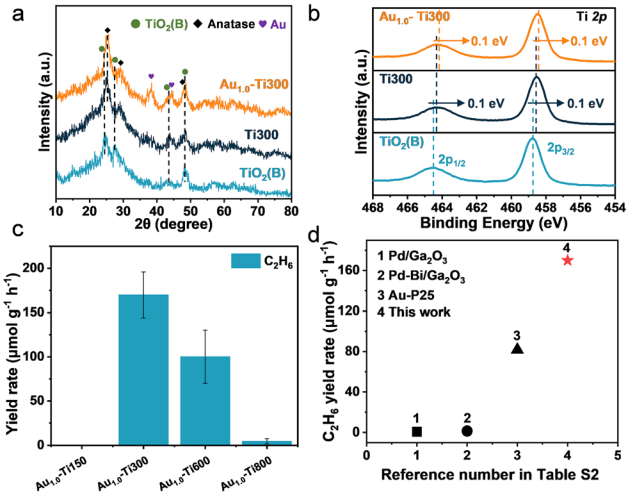

Fig. 2 (a) XRD patterns of TiO_2(B) NSs, Ti300, and $Au_{1.0}$–Ti300. (b) Ti 2p high-resolution XPS spectra of related samples. (c) The production rate of C_2H_6 for photocatalytic CH_4 coupling over $Au_{1.0}$–Ti with different calcination temperatures. (d) The comparison of C_2H_6 yield rate of recently published references using flow reactors.

X-ray photoelectron spectroscopy (XPS) was used to characterize the chemical states. Ti, O, and C were detected in all samples (Fig. S7, ESI†); the peak of Au was not obvious owing to its low content. XPS confirmed the existence of Ti^{4+} in all samples.[22] The lower binding energy of the Ti 2p peaks for Ti300 suggests a lower oxidation state of Ti, indicating the self-doping of Ti^{3+} arising from phase contact (Fig. 2(b)).[23] With Au loading, the binding energies of the Ti 2p peaks decreased by ∼0.1 eV, suggesting that more electrons moved into the Ti sites. O 1s spectra revealed different oxygen species (Fig. S8a, ESI†),[21,24] and a decrease in hydroxyl groups after heat treatment indicates an increase in available adsorption sites. Au 4f peaks confirmed the presence of metallic Au NPs (Fig. S8b, ESI†).[25]

Photocatalytic performance was tested using a homemade flow-cell system (Fig. S9, ESI†). Pure TiO_2(B) loaded with Au (*i.e.* $Au_{1.0}$–Ti150) produced almost no C_2H_6 (Fig. 2(c)), highlighting the essential role of anatase in regulating the strong over-oxidative ability of Au–TiO_2(B). $Au_{1.0}$–Ti300 exhibited the highest photocatalytic C_2H_6 yield rate (170 μmol g^{-1} h^{-1}). $Au_{1.0}$–Ti600 did not have better catalytic performance for C_2H_6 production, probably due to the weaker oxidation ability of pure anatase compared to the homojunction, which diminished its capacity to activate CH_4. An increase in the rutile ratio further reduced the photocatalyst activity, with no C_2H_6 produced from $Au_{1.0}$–Ti800. The optimal Au loading on Ti300 was 1.0 wt% (Fig. S10, ESI†). Notably, the $Au_{1.0}$–Ti300 catalyst exhibited the highest C_2H_6 yield rate among state-of-the-art photocatalytic NOCM reactions using flow-cell reactors (Fig. 2(c) and Table S2, ESI†).

No H_2 was detected in this photocatalytic system, probably because of the consumption of lattice oxygen on the surface of TiO_2, which led to the production of surface-adsorbed oxygen species or water. Additionally, the reaction involving lattice oxygen produces CO and CO_2 as by-products of CH_4 overoxidation (Fig. S11, ESI†), resulting in a C_2H_6 selectivity (carbon

Published on 06 November 2024. Downloaded on 3/3/2026 11:38:33 PM.

balance selectivity) of 45%. Fig. S12 (ESI†) illustrates the photocatalytic performance of $Au_{1.0}$–Ti300 over 2 h. The C_2H_6 yield rate became stable at 90 min and the CO_2 yield rate gradually declined after 30 min of irradiation, suggesting possible consumption of surface lattice oxygen. The cycling stability test of $Au_{1.0}$–Ti300 is shown in Fig. S13 (ESI†). To regenerate the lost lattice oxygen,[26] the catalyst was exposed to air for 2 h in each cycle. The performance of $Au_{1.0}$–Ti300 did not decrease significantly after four cycles, suggesting rapid lattice oxygen regeneration capability and good stability of the TiO_2(B)–anatase homojunction. TEM images reveal that the NS morphology of the catalyst remained unchanged after the reaction (Fig. S14, ESI†), and the average size of the Au NPs increased to ~14 nm, possibly owing to the heating agglomeration from long-term illumination.

Control experiments were conducted to gain a better understanding of the structure–activity relationship of the components in $Au_{1.0}$–Ti300 (Fig. S15, ESI†). With no CH_4 source, no products were detected, confirming that carbon products originated from CH_4 rather than organic residues. Under visible-light illumination, only a small amount of CO_2 was produced, indicating that the localized surface plasmon resonance effect of Au did not influence this reaction, and that the dehydrogenation of CH_4 to methyl radicals ($CH_3^{\bullet}$) mainly occurred on the TiO_2 surface rather than on Au. $Au_{1.0}$–Ti150 had significantly higher activity than Ti150, showing Au's role in enhancing electron–hole pair separation. No C_2H_6 was produced without Au, highlighting its necessity for coupling methyl radicals. The ternary system of $Au_{1.0}$–Ti300, with a balanced anatase/TiO_2(B) ratio, showed enhanced performance by suppressing over-oxidation and facilitating C_2H_6 production, outperforming commercial P25 TiO_2 by a factor of 1.6.

Photoluminescence (PL), transient photocurrent, and electrochemical impedance spectroscopy (EIS) were used to assess electron–hole separation in the catalysts. PL spectra (Fig. S16a, ESI†) revealed that $Au_{1.0}$–Ti300 had weaker PL intensity than Ti300, indicating longer carrier lifetimes. Ti300 has a higher photocurrent density than pristine TiO_2(B) (Fig. S16b, ESI†), demonstrating effective electron–hole separation due to the homojunction structure. Au further promotes charge transfer between TiO_2(B) and anatase, which is in agreement with the XPS results. The EIS results also exhibited a trend consistent with the transient photocurrent response (Fig. S16c and Table S3, ESI†), in which the Au and homojunction decreased the transfer resistance of the photogenerated charges.

According to the UV-vis DRS and the corresponding Tauc plot (Fig. S3, ESI†), the energy band gaps (E_g) of TiO_2(B) and anatase were calculated to be 3.69 eV and 3.38 eV, respectively. The valence band maxima (VBM) of TiO_2(B) and anatase are located at 2.97 eV and 2.49 eV, respectively (Fig. 3). Consequently, the estimated conductive band minimum (CBM) of TiO_2(B) and anatase are calculated to be −0.72 and −0.89 eV, which are consistent with the flat band potentials of TiO_2(B) and anatase determined through Mott–Schottky measurements (Fig. S17, ESI†). Through combining the band structure analysis and XPS results, possible type-II and Z-scheme band structures were proposed (Fig. 3(c)). Interestingly, the introduction of water vapor

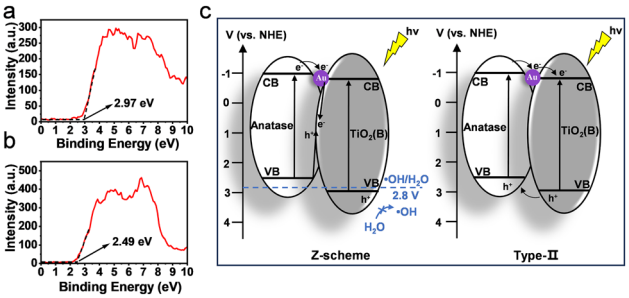

Fig. 3 Energy band structure. (a) VB-XPS spectrum of TiO_2(B). (b) VB-XPS spectrum of anatase TiO_2. (c) Schematic illustration of the energy band structure of $Au_{1.0}$–Ti300.

into the photocatalytic system did not alter product distributions or yield rates (Fig. S18, ESI†). This proves that water cannot be oxidized to hydroxyl radicals ($E^0(^{\bullet}OH/H_2O)$ = 2.8 V) over the TiO_2 homojunction structure.[27] Thus, the type-II structure is preferred over the Z-scheme structure, which retains the undesirably strong oxidation capacity of TiO_2(B).

In situ diffuse-reflectance infrared Fourier transform spectroscopy (DRIFTS) was employed to detect the reaction intermediates and reveal the reaction pathway. Peaks at 1536 cm^{-1}, corresponding to the symmetric stretching vibrations of CH_4, emerged upon light irradiation, indicating enhanced CH_4 adsorption on the TiO_2 surface.[11,28] Vibration modes related to CH_3/CH_2 deformation at 1475 cm^{-1}, 1465 cm^{-1}, and 1448 cm^{-1} (Fig. S19, ESI†) suggest that adsorbed CH_4 undergoes dehydrogenation on the TiO_2 surface.[29,30] These signals become stronger for $Au_{1.0}$–Ti300 (Fig. 3(b)), indicating that the loading of Au NPs improves overall CH_4 activity. Additionally, C–O stretching vibrational modes at 1016 and 1009 cm^{-1}, assigned to CO_2 formation, appeared in both catalysts, demonstrating the over-oxidation of CH_4 on the TiO_2 catalyst surface. Furthermore, a small signal at 865 cm^{-1} assigned to the C–C stretching mode of C_2H_6 was only in $Au_{1.0}$–Ti300.[30,31] This shows that Au dominates the coupling stage of CH_4, which is consistent with the results of the control experiments.

Based on the aforementioned photocatalytic CH_4 performance, energy band structure analysis, and DRIFTS results, we propose a schematic of the possible reaction routes for the photocatalytic NOCM to C_2H_6 on $Au_{1.0}$–Ti300 (Fig. 4). First, CH_4 is adsorbed onto the surface of TiO_2 in the dark. Upon irradiation, electron–hole pairs are generated within TiO_2. Subsequently, dehydrogenation of CH_4 occurs on the TiO_2 surface, and lattice oxygen is converted to O^- by hole induction, trapping protons from adjacent adsorbed CH_4 to form methyl radicals attached to the Ti sites. The O^- sites tend to trap methyl radicals to form intermediate species such as $^*CH_3O$ or $^*CH_2O$, which can further be overoxidized to CO and CO_2. In addition, surface O sites that trap one proton can subsequently trap a second proton from CH_4, resulting in water generation. Consequently, lattice oxygen is removed along with water or over-oxidative products when they are dissociated from the catalyst surface to leave oxygen vacancies. In this process, the homogeneous heterojunction enables TiO_2(B) to exhibit a more moderate oxidation ability, reducing the CO_2 generation.

 This journal is © The Royal Society of Chemistry 2024

Published on 06 November 2024. Downloaded on 3/3/2026 11:38:33 PM.

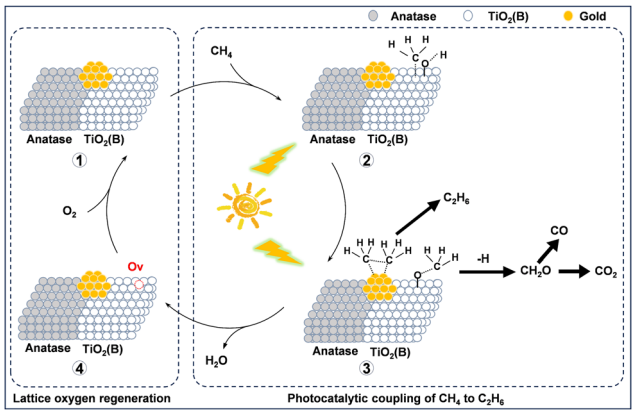

Fig. 4 Schematic illustration for photocatalytic CH_4 conversion in the case of $Au_{1.0}$–Ti300.

Besides, during the charge-transfer process, some electrons that avoid charge recombination pass through the Au NPs, resulting in the negatively charged Au surface capturing dissociative methyl radicals and protecting them from overoxidation. Finally, the coupling of the methyl radicals results in the formation and desorption of free C_2H_6 into the gas flow. The lost lattice oxygen can be easily regenerated in an oxygen-rich atmosphere for another catalytic cycle.

In summary, the TiO_2-based hybrid photocatalyst achieves efficient conversion of CH_4 to C_2H_6 at a rate of 170.0 μmol g^{-1} h^{-1} in a flow reactor. The dehydrogenation of CH_4 occurs over TiO_2 with a relatively moderate oxidative ability owing to the formation of type-II homojunctions between the TiO_2(B) and anatase phases. Au plays a critical role not only in promoting charge mitigation but also in coupling methyl radicals. The catalyst highlights the ternary synergistic effect in photocatalytic CH_4 coupling, providing insights for future catalyst design and industrial CH_4 conversion.

X. L., H. L., B. X., and Z. L. designed and conducted the experiments, analyzed the results, and drafted the manuscript. Y. C., K. L., X. Y., L. X., and T. G. contributed to the discussion of the results. Y. Z. and W. Z. supervised the project, engaged in discussions, and revised the manuscript.

Y. Z. would like to acknowledge the support from the National Natural Science Foundation of China (22276100), Natural Science Foundation of Jiangsu Province (BK20220405), Research Fund for Jiangsu Distinguished Professor (RK030STP22001), and Key Laboratory for Organic Electronics & Information Displays (GZR2024010003). W. Z. would like to acknowledge the support from the National Natural Science Foundation of China (22176086), Research Funds for Jiangsu Distinguished Professor, Carbon Peaking and Carbon Neutrality Technological Innovation Foundation of Jiangsu Province (BE2022861), the Research Funds from Frontiers Science Center for Critical Earth Material Cycling of Nanjing University, State Key Laboratory of Pollution Control and Resource Reuse, and the Fundamental Research Funds for the Central Universities (021114380214, 021114380222).

Data availability

The data supporting this article have been included as part of the ESI.†

Conflicts of interest

There are no conflicts to declare.

Notes and references

1 S. A. Montzka, E. J. Dlugokencky and J. H. Butler, *Nature*, 2011, **476**, 43–50.
2 S. Wang, P. Sun, G. Zhang, N. Gray, J. Dolfing, S. Esquivel-Elizondo, J. Peñuelas and Y. Wu, *Innovation*, 2022, **3**, 100192.
3 Q. Zhan, Y. Kong, X. Wang and L. Li, *Chem. Commun.*, 2024, **60**, 2732–2743.
4 N. F. Dummer, D. J. Willock, Q. He, M. J. Howard, R. J. Lewis, G. Qi, S. H. Taylor, J. Xu, D. Bethell, C. J. Kiely and G. J. Hutchings, *Chem. Rev.*, 2023, **123**, 6359–6411.
5 J. Fu, P. Li, Y. Lin, H. Du, H. Liu, W. Zhu and H. Ren, *Eco-Environ. Health*, 2022, **1**, 259–279.
6 X. Lu and V. Valtchev, *Green Carbon*, 2023, **1**, 1.
7 X. Li, C. Wang and J. Tang, *Nat. Rev. Mater.*, 2022, **7**, 617–632.
8 A. Gao and L. Gu, *Innov. Mater.*, 2023, **1**, 100009.
9 M. Cai, Y. Wei, Y. Li, X. Li, S. Wang, G. Shao and P. Zhang, *EcoEnergy*, 2023, **1**, 248–295.
10 P. Wang, R. Shi, J. Zhao and T. Zhang, *Adv. Sci.*, 2024, **11**, 2305471.
11 W. Jiang, J. Low, K. Mao, D. Duan, S. Chen, W. Liu, C.-W. Pao, J. Ma, S. Sang, C. Shu, X. Zhan, Z. Qi, H. Zhang, Z. Liu, X. Wu, R. Long, L. Song and Y. Xiong, *J. Am. Chem. Soc.*, 2021, **143**, 269–278.
12 Z. Liu, B. Xu, X. Lu, P. Li, J.-J. Zhu and W. Zhu, *Mater. Chem. Front.*, 2024, **8**, 2161–2172.
13 A. Meng, L. Zhang, B. Cheng and J. Yu, *Adv. Mater.*, 2019, **31**, 1807660.
14 D. Fattakhova-Rohlfing, A. Zaleska and T. Bein, *Chem. Rev.*, 2014, **114**, 9487–9558.
15 Y. Chen, S. Tang, L. Li, X. Liu and J. Liang, *ACS Sustainable Chem. Eng.*, 2023, **11**, 3568–3575.
16 L. Sheng, T. Liao, L. Kou and Z. Sun, *Mater. Today Energy*, 2017, **3**, 32–39.
17 G. Xiang, T. Li, J. Zhuang and X. Wang, *Chem. Commun.*, 2010, **46**, 6801–6803.
18 W. Guo, Y. Qin, C. Liu, B. Guo, J. Zou, Z. Xie and L. Wu, *Appl. Catal., B*, 2021, **298**, 120526.
19 J. Wang, H. Jia, Y. Guo, Y. Zhang, Q. Xie, H. Zhu, J. Sun, F. Shi, Z.-H. Liu and R. Jiang, *Sol. RRL*, 2019, **3**, 1900323.
20 S. Linic, U. Aslam, C. Boerigter and M. Morabito, *Nat. Mater.*, 2015, **14**, 567–576.
21 X. Luo, Y. Su, Y. Wang, K. P. Homewood, X. Chen, R. Li and Y. Gao, *Appl. Surf. Sci.*, 2021, **567**, 150837.
22 K. Li, Y. Cai, X. Yang, S. Wang, C. Teng, Y. Tian, Q. Min and W. Zhu, *Adv. Funct. Mater.*, 2022, **32**, 2113002.
23 G. Wang, S. Zhang, R. Qian and Z. Wen, *ACS Appl. Mater. Interfaces*, 2018, **10**, 41398–41406.
24 G. Xiang, Y.-G. Wang, J. Li, J. Zhuang and X. Wang, *Sci. Rep.*, 2013, **3**, 1411.
25 J. Lang, Y. Ma, X. Wu, Y. Jiang and Y. H. Hu, *Green Chem.*, 2020, **22**, 4669–4675.
26 H. Du, H. Luo, M. Jiang, X. Yan, F. Jiang and H. Chen, *Appl. Catal., A*, 2023, **664**, 119348.
27 H. Song, X. Meng, S. Wang, W. Zhou, S. Song, T. Kako and J. Ye, *ACS Catal.*, 2020, **10**, 14318–14326.
28 X. Yu, V. De Waele, A. Löfberg, V. Ordomsky and A. Y. Khodakov, *Nat. Commun.*, 2019, **10**, 700.
29 X. Chen, Y. Li, X. Pan, D. Cortie, X. Huang and Z. Yi, *Nat. Commun.*, 2016, **7**, 12273.
30 W. Zhang, C. Fu, J. Low, D. Duan, J. Ma, W. Jiang, Y. Chen, H. Liu, Z. Qi, R. Long, Y. Yao, X. Li, H. Zhang, Z. Liu, J. Yang, Z. Zou and Y. Xiong, *Nat. Commun.*, 2022, **13**, 2806.
31 J. Wang, Y. Peng and W. Xiao, *Sci. China: Chem.*, 2023, **66**, 3252–3261.